Quantum dynamics in the highly discrete, commensurate Frenkel Kontorova model: A path-integral molecular dynamics study

Florian R. Krajewski*
Computational Science, Department of Chemistry and Applied Biosciences, ETH Zurich, USI Campus, Via Giuseppe Buffi 13, CH-6900 Lugano, Switzerland and Institut für Physik, WA 331, Johannes Gutenberg-Universität Mainz, 55099 Mainz, Germany

Martin H. Müser†
Department of Applied Mathematics, University of Western Ontario, London, Ontario N6A 5B7, Canada‡
(Dated: November 5, 2004)

The commensurate Frenkel Kontorova (FK) model is studied with path-integral molecular dynamics (PIMD). We focus on the highly discrete case, in which the embedding potential has a much greater maximum curvature than the harmonic potential connecting two particles in the FK chain. Using efficient sampling methods, the dynamical interpretation of adiabatic PIMD appears to represent quite accurately the true time correlation functions of this highly-correlated many-body system. New behavior is found in the quantum FK model with respect to its continuum solution. In the pinned phase ($m > m_c$), the spectral density does not show the characteristic $\omega^{-2}\Theta(\omega - \omega_c)$ cusp of the continuum solution. We also identify a dynamical quantum hysteresis in addition to the regular classical hysteresis when an external force is applied to the FK chain. In the unpinned phase ($m \leq m_c$), we find a linear response damping coefficient which is finite and only weakly dependent on temperature T at small values of T.

PACS numbers: 05.60.Gg, 71.10.Pm, 73.43.Jn

I. INTRODUCTION

The sine-Gordon (SG) model describes the motion of an elastic object through an external potential. The model is also known as Frenkel-Kontorova (FK) model [1, 2] if the degrees of freedom consist of discrete mass points. Thus the SG model is the continuum approximation of the FK model. The SG model has been applied to charge-density waves in solids, coupled Josephson junctions [3], the sliding motion of an adsorbed layer of atoms over a substrate [4], and most recently electronic conductance in nanotubes [5], see also the reviews [6, 7] on electronic transport in one-dimensional structures. The SG model is also a prototypical model to describe the transition from a metal to a Mott insulator [8]

A lot of attention has been devoted to the (discrete) classical FK model both at zero and finite temperatures [2, 3] and the (continuum) quantum-mechanical SG model [7, 9]. However, less is known about the quantum-mechanical properties of the *discrete* quantum FK (QFK) model, in particular about its *dynamical* properties. Numerical approaches have lead to a clear picture, how quantum fluctuations renormalize the thermal equilibrium structure, but results are often limited to zero (or small) external fields [10] or to variational approaches [11]. While quantum Monte Carlo methods yield numerically exact results for static properties [12, 13], they only allow one to calculate small-frequency dynamical properties indirectly, i.e., by drawing conclusion on the existence of a phonon gap by studying the temperature dependence of the internal energy. It can also be helpful within quantum Monte Carlo approaches to use *a priori* information on the functional form of the low-energy spectrum [14, 15]. This has been done recently for the analysis of phonon and instanton dispersions in the incommensurate SG model [15]. Appropriate imaginary-time correlation functions were fitted to the Wick rotated spectrum of single or double harmonic oscillators. The approach works well if the damping is sufficiently small and a clear frequency separation between phonons and instantons is given. However, it is not universally applicable.

One of the reasons why little is known about the interesting dynamics of the discrete QFK model is that many-body, long-time dynamics are typically difficult to compute. All established, numerically exact algorithms known to the authors (i.e. algorithms in which the systematic and/or stochastic error can be made arbitrarily small in principle) scale exponentially with system size and time scale. However, advances have been claimed for the calculation of time correlation functions in thermal equilibrium: It was suggested that real time correlation functions $C(t)$ of observables linear in velocity v and/or position x can be calculated exactly within the framework of adiabatic path integral molecular dynamics (PIMD) [16, 17]. If this claim was true, then it would be possible to calculate dynamical response functions, including long-time dynamics of many-body systems, such that only (controllable) stochastic errors would persist. For instance, it would be possible to address the ques-

*florian.krajewski@phys.chem.ethz.ch
†mmuser@uwo.ca
‡http://publish.uwo.ca/~mmuser/

tion whether the (high) discreteness of a FK chain can alter the universal behavior of the continuous SG model. However, concerns have been raised regarding the reliability of the method for strongly correlated [18] and for strongly anharmonic [19] systems. At this point, it is only established that the leading corrections to centroid correlation functions are at the most in the order of $\hbar^4$ for anharmonic but well-behaved potentials and that no corrections apply to correlation functions related to harmonic variables.

Path integral molecular dynamics is a method to calculate static [20] and dynamic [21] properties of many-body quantum systems in thermal equilibrium. It is based on the isomorphism between the partition function of a quantum mechanical point particle and that of a classical ring polymer. The number of monomers per ring is called Trotter number P. As mentioned above, it was suggested that real time correlation functions $C(t)$ of observables linear in velocity v and/or position x can be calculated exactly with adiabatic PIMD methods [16, 17]. The $C(t)$'s follow from the equivalent correlation functions $C_{\rm c}(t)$ defined for the ring polymer's centroids (center of mass), provided that the $P-1$ inner degrees of freedom are in full thermodynamic equilibrium for every given position of the centroids. Furthermore, the characteristic time constant of the centroids' thermostats must be large compared to the intrinsic relaxation time of the system. If these two conditions are satisfied, $C(t)$'s and $C_{\rm c}(t)$'s Fourier transforms are related through the equation $\tilde{C}(\omega) = \beta\hbar\omega/2(\coth(\beta\hbar\omega/2)+1)\tilde{C}_{\rm c}(\omega)$, where β is the inverse thermal energy. In the following, only centroid spectra $\tilde{C}_{\rm c}(\omega)$ will be considered, as they reflect directly the density of states.

In a previous paper, we applied regular PIMD and adiabatic PIMD to the discrete sine Gordon or Frenkel Kontorova model [22]. We could show that a gap in the dispersion relation at infinite wave length opened up when the physical masses of the FK particles exceeded a critical mass m_c. The value of m_c was close to the value predicted by the exact solution of the continuum model.

In this study, we extend the presentation of our previous paper by describing algorithm and implementation in detail. The present study contains new results on the density of states as well as an analysis of the self-consistency of imaginary-time correlation functions and centroid spectra. Moreover, the dynamical response to an external driving force will be investigated. Since some of the force-velocity relationship exhibited discontinuous behavior, it is natural to address the question of dynamical hysteresis, i.e., to investigate whether different steady-state responses exist for a given external force depending on the previous history of the chain.

We also wish to mention a recent quantum Monte Carlo study done on a similar quantum transition for the incommensurate QFK model [15] in which a critical mass m_c was identified as well. It contains a thorough analysis of the role of instantons at the transition. An important difference between the commensurate QFK model and the incommensurate QFK model is that there is a well-defined ground state in the pinned regime with a degeneracy that only scales linearly with system size N in the commensurate case. Conversely, the degeneracy in the pinned incommensurate system scales exponentially with N. Due to this qualitative difference, we will not make a detailed comparison to that study and neither comment in depth on the disordered QFK model, which was studied numerically by the present authors [22, 23].

The remainder of this paper is organized as follows. In the next section, we will describe the model Hamiltonian and our algorithm. This includes the derivation of our method, in which all harmonic interactions of the system are diagonalized and in which leading errors of the full system only occur in order $1/P^4$. We also describe how critical slowing down with system size can be suppressed and how estimators for thermodynamic averages have to be redefined in the new schemes. In Sec. III, we will present our results. We will conclude in Sec. IV.

II. MODEL AND METHOD

A. Model Hamiltonian

The Hamilton operator analyzed in this study reads

$$\hat{H} = \sum_{j=0}^{N-1} \left(\underbrace{\frac{\hat{p}_j^2}{2m} + \frac{K}{2}\left(\hat{x}_j + 2\pi b - \hat{x}_{j+1}\right)^2}_{Q} - \underbrace{V_0 \cos(\hat{x}_j/b)}_{R} \right), \tag{1}$$

where $\hat{p}_j$ and x_j are, respectively momentum and position of particle j, K is the stiffness of the spring connecting two neighbored particles, V_0 is the coupling strength to the embedding system, and $2\pi b$ is the substrate's lattice constant. The periodic boundary condition $x_{n+N} = x_n + 2\pi bN$ makes the chain commensurate with the substrate. (Due to the periodic boundary conditions the term $2\pi b$ on the r.h.s. of Eq. (1) is not necessary, but it is included in order to avoid confusion.) Our system of units will be defined by V_0, b, $\hbar$, and Boltzmann's constant k_B. All these quantities will be to unity. They will be suppressed in some of the following formulae. Unless otherwise noted, we vary the mass m but leave the harmonic intrachain coupling $K = 0.1\ V_0/b^2$ constant.

The Hamiltonian can be interpreted as a harmonic chain (contribution Q in the Hamiltonian) on a sinusoidal substrate potential (contribution R). The model roughly mimics the behavior of electrons in one-dimensional structures: Due to the Fermi principle, the topology of the nodal structure is known and as a consequence of the nodal structure, electrons cannot pass each other in 1D. In the FK model, this effect is taken care off by the harmonic springs. If no harmonic interactions between the chain particles were present, then the ground state of an individual particle would be a simple Bloch state, just like that of an independent electron in a periodic

potential.

Many exact results exist for the continuum approximation of the SG model, i.e., the value of the mass m_c above which the chain is a conductor, exponents describing the density of states, etc. However, the validity of continuum approximations can be challenged when the maximum curvature of the potential, namely V_0/b^2 exceeds the stiffness K of the springs. For example, solitons behave qualitatively different in the classical SG model and the classical FK model: In the (continuum) SG model, solitons move frictionless through the system, while in the (discrete) FK model, solitons couple to the phonon bath and thus experience a drag force. In this study, we will be concerned with a highly discrete system, as the ratio of elastic coupling and maximum potential curvature is small, namely $Kb^2/V_0 = 0.1$.

B. Simulation algorithm

The determination of the quantum statistical and dynamic properties in the framework of path integral simulation remains challenging, despite increasing computing power. It would probably be unfeasible to obtain high-resolution data if the computations were based on standard path integral algorithms. In order to reduce the finite-P quantum corrections, large Trotter numbers are required. As we are interested in a transition between pinned and unpinned chain, it is necessary to go to large system sizes, which typically leads to critical slowing down. Even in the absence of a phase transition, i.e. deep in the conducting phase, an effectively free chain shows Rouse dynamics and correlation times of the slowest mode (the center of mass mode) become tremendously large.

We will therefore be concerned with the derivation of a hybrid algorithm that incorporates simultaneously different approaches that render path integral simulations more efficient. To the best of our knowledge, there has not yet been a report of such a combination of algorithms in the literature. The following three steps were taken (simultaneously) in the present study:
(*i*) The Hamiltonian is split into a harmonic part, which is quadratic in the operators $\hat{x}$ and $\hat{p}$, and in a rest part (quadratic-rest decomposition QR) [24, 25]. The harmonic part is treated exactly by the analytic solution.
(*ii*) Once the Hamiltonian is decomposed into two contributions $\hat{H} = \hat{H}_0 + V_1$, decompositions of the high-temperature density matrix will be done such that Takahashi Imada corrections [26] are included. This leads to a convergence with $1/P^4$.
(*iii*) For the calculation of static properties in PIMD, it is possible to choose the dynamical masses at will [20]. This can be done such that the eigenmodes of the unperturbed system described by $\hat{H}_0$ all move on the same time scale [27]. Previously, this Fourier speed up had only been applied in the case where $\hat{H}_0$ was the kinetic energy, but it is of course possible, to do the same for a more complex case such as $\hat{H}_0 = Q$.

The next three subsections will be concerned with the details of these three items. Points (*i*) and (*ii*) are also useful for path integral Monte Carlo (PIMC), however, the advantages due to the speed up related to item (*iii*) cannot be implemented in PIMC in a straightforward fashion, even if the exact solution of the SG model was exploited in PIMC. The algorithms introduced in Sects. (II B 1) and (II B 2) will put forth temperature-dependent effective potentials. This makes it necessary to redefine the expressions that need to be averaged to yield thermodynamic averages. Such expressions are called estimators and they will be discussed in Sec. II C

1. *Splitting off harmonic interactions*

It has been realized a long time ago that it is often beneficial to split off the harmonic contributions in path integrals and to evaluate harmonic fluctuations around the classical path exactly [24]. Non-harmonic fluctuations can then be dealt with numerically or perturbatively. This idea is not limited to the FK model but can be applied to all systems in which a harmonic approximation can be meaningfully defined [25]. This is why we chose a more general representation at this point. Examples for such systems are crystals and molecules, for which the harmonic approximation can be solved analytically once the interactions between the atoms are known.

Starting point is the N-particle Hamiltonian

$$H = \sum_{j=0}^{N-1} \frac{\hat{p}_j^2}{2m_j} + V\left(\{\hat{x}_j\}\right) \tag{2}$$

with a potential V that can be is decomposed into a harmonic part V_{harm} and a rest part V_{I}:

$$V\left(\{\hat{x}_j\}\right) = \sum_{j,j'=0}^{N-1} \frac{1}{2}\hat{x}_j W_{j\,j'}\,\hat{x}_{j'} + V_{\mathrm{I}}\left(\{\hat{x}_j\}\right) \ . \tag{3}$$

$W_{j\,j'}$ is a symmetric real matrix which can be diagonalized by an orthogonal transformation A. The harmonic interaction of neighbored particles can be diagonalized with a normal mode transformation. In terms of the new eigencoordinates $q_k = \sum_j A_{kj}x_j$ of the matrix W, the Hamiltonian reads:

$$\begin{aligned}\hat{H} &= \sum_{k=0}^{N-1}\left(\frac{\hat{p}_k^2}{2m_k} + \frac{1}{2}K_k q_k^2\right) + V_{\mathrm{I}}\left(\{q_k\}\right) \\ &=: \sum_{k=0}^{N-1}\left(\hat{T}_{\mathrm{kin},k} + V_{\mathrm{harm},k}\right) + V_{\mathrm{I}}\left(\{q_k\}\right) \ . \end{aligned} \tag{4}$$

Here, k enumerates the eigenmodes and the coefficients K_k are the eigenvalues of the matrix W. q_k is the amplitude associated with the motion of eigenmode k, m_k the corresponding inertia, and $\hat{T}_{\mathrm{kin},k}$ and $V_{\mathrm{harm},k}$ are kinetic and potential energy of eigenmode k.

This decomposition is inserted into the primitive decomposition of the high-temperature density matrix $\exp[-\beta(H_0+V_{\rm I})/P] \approx \exp[-\beta H_0/P]\exp[-\beta V_{\rm I}/P]$. The partition function can now be written as:

$$Z(\beta) = \lim_{P\to\infty}\int\prod_{\tau=0}^{P-1}\prod_{k=0}^{N-1} dq_k^\tau \cdots \langle\{q_k\}^\tau|e^{-\beta\left(\hat{T}_{\rm kin}+V_{\rm harm}\right)/P}e^{-\beta V_{\rm I}/P}|\{q_k\}^{\tau+1}\rangle \quad (5)$$

with $\hat{T}_{\rm kin}$ and $V_{\rm harm}$ the net kinetic energy and net harmonic potential, respectively. q_k^τ denotes the value of the amplitude of the k'th eigenmode at imaginary time τ. The partition function can be simplified further if one realizes that the perturbation $V_{\rm I}$ and the amplitudes of the eigenmodes are both diagonal in real space. The non-trivial part of the calculation is the evaluation of the high-temperature density matrix elements $\rho_{\rm Q}$ associated with the quadratic (Q) Hamiltonian, i.e.,

$$\rho_{{\rm Q},k,\tau}\left(\frac{\beta}{P}\right) =< q_k^\tau|e^{-\frac{\beta}{P}(\hat{T}_{{\rm kin},k}+V_{{\rm harm},k})}|q_k^{\tau+1}> . \quad (6)$$

The result of this expression is well-known and is given by:

$$\rho_{{\rm Q},k,\tau}\left(\frac{\beta}{P}\right) = \sqrt{\frac{1}{2\pi\sigma_k^2}}\, e^{-\left(q_k^\tau-q_k^{\tau+1}\right)^2/2\sigma_k^2} \times e^{-\frac{\beta}{2P}\kappa_k\left((q_k^\tau)^2+(q_k^{\tau+1})^2\right)/2} \quad (7)$$

with

$$\sigma_k = \sqrt{\frac{\hbar^2\beta}{m_k P}\frac{\sinh(f_k)}{f_k}} \quad (8)$$

$$\kappa_k = K_k\frac{2\tanh(f_k/2)}{f_k} \quad (9)$$

and

$$f_k = \frac{\hbar\beta}{P}\sqrt{\frac{K_k}{m}}. \quad (10)$$

Terms resulting from summing up over τ the different contributions $(q_k^t - q_k^{t+1})^2$ in the exponent on the r.h.s. of Eq. (7) can be diagonalized with an additional normal mode transformation U along the imaginary-time axis. This transformation is that of a linear elastic chain in an external harmonic potential of stiffness κ_k, thus

$$U_{\Omega\tau} = \sqrt{\frac{1}{P}}\exp\left(2\pi i\Omega\tau/P\right). \quad (11)$$

For the new normal coordinates

$$u_k^\Omega = \sum_\tau U_{\Omega\tau}q_k^\tau \quad (12)$$

$$= \sum_{\tau,j} U_{\Omega\tau}A_{kj}x_j^\tau, \quad (13)$$

the final (and exact) result for the diagonalized partition function $Z_{\rm Q}(\beta)$ at zero perturbation $V_{\rm I}=0$ is given by

$$Z_{\rm Q}(\beta) = \prod_{\Omega=0}^{P-1}\prod_{k=0}^{N-1}\int\frac{du_k^\Omega}{\sqrt{2\pi\sigma_k^2}}\; e^{-\frac{\beta}{P}\tilde{\kappa}(k,\Omega)|u_k^\Omega|^2/2}. \quad (14)$$

where the effective spring constant $\tilde{\kappa}(k,\Omega)$ belonging to eigenmode u_k^Ω can be written as:

$$\tilde{\kappa}(k,\Omega) = \kappa_k + \frac{4P}{\sigma_k^2\beta}\sin^2(\pi\Omega/P). \quad (15)$$

The factorization of the harmonic modes shown above can be used for the calculation of the partition function Eq. (6). The non-harmonic term $V_{\rm I}$, whose natural presentation is in x_j^τ rather than in the u_k^Ω has to be evaluated by inverting the normal mode transformation Eq (13).

We will conclude this subsection by sketching the calculation of the relevant coefficients for the FK model. $V_{\rm I}$ and $W_{jj'}$ correspond to

$$V_{\rm I} = -V_0\sum_{j=0}^{N-1}\cos\left(x_j/b\right), \quad (16)$$

$$W_{jj'} = K\left(2\delta_{jj'}-\delta_{j(j'+1)}-\delta_{(j+1)j'}\right). \quad (17)$$

The regular Fourier analysis of a linear elastic chain [see also Eq. (11)] then shows that the normal model coefficients m_k and K_k are given by

$$m_k = m \quad (18)$$

$$K_k = 4K\sin^2\left(\pi k/N\right) \quad (19)$$

from which all the other terms follow.

2. *Reducing the error to* $1/P^4$

While the manipulations in Sec. II B 1 decrease the absolute error when evaluating the partition function for finite Trotter numbers P, they do not improve the convergence rate in the sense that the leading-order corrections remain $\mathcal{O}(1/P^2)$, albeit with a reduced prefactor. However, it is possible to improve the situation by including correction terms originally suggested for spin systems [28]. The idea is to approximate the partition function of a Hamiltonian $\hat{H} = \hat{H}_0 + V_1$ as

$$Z(\beta) = {\rm Tr}\; e^{-\beta\hat{H}} \approx {\rm Tr}\;\left(e^{-\beta\hat{H}_0/P}e^{-\beta\hat{V}_1/P}e^{-\beta V_{\rm cor}/P}\right)^P \quad (20)$$

with

$$V_{\rm cor} = \frac{\beta^2}{24P^2}[V_1,[H_0,V_1]] \quad (21)$$

and a leading error of the order $\mathcal{O}\left(P^{-4}\right)$. where $[A,B]$ denotes the commutator of the operators A and B.

Takahashi and Imada applied these corrections to translational degrees of freedom. If one associates H_0 with the kinetic energy and V_1 with the net potential energy, the correction term is diagonal in real space. It is given by

$$V_{\rm cor} = \frac{\beta^2\hbar^2}{12mP^2} \mid \nabla_j V_1 \mid^2, \tag{22}$$

where ∇_j is the gradient of V_1 with respect to particle j, i.e., in one dimension $\partial/\partial x_j$. It could be shown that finite-P corrections are of order $1/P^4$ for a large class of potentials, including the strongly repulsive 12-6 Lennard Jones potential [29].

The Takahashi Imada scheme is easily applied to the QR decomposition from Sec. II B 1 as well, since the harmonic potential energy commutes with the anharmonic potential energy, i.e., $[T_{\rm kin}+V_{\rm harm}, V_{\rm I}] = [T_{\rm kin}, V_{\rm I}]$. Thus, in the QR decomposition combined with the Takahashi Imada scheme, we simply have to associate V_1 with $V_{\rm I}$ in Eqs. (21) and (22). For the calculation of forces in a PIMD simulation, it is convenient to calculate the correction potential and the forces associated with $F_k^\Omega = \partial V_{\rm cor}/\partial u_k^\Omega$ in the original representation x_j^τ and to transform the forces into the reciprocal space using Eq. (11). This transformation is most efficiently done using fast Fourier transforms.

We will now demonstrate the convergence rates in the various approaches. For this purpose, we compare the so-called primitive algorithm (PA), the quadratic-rest decomposition without higher-order correction (QR), the pure higher-order propagator (HOA) without QR (which is also called Takahashi Imada approach) and the combined QR-HOA approach. To remind the reader, PA is based on the decomposition of the high-temperature density matrix outlined in Eq. (20) *without* including the correction terms $V_{\rm cor}$ and by associating respectively $\hat{H}_0$ with $\hat{T}_{\rm kin}$ and V_1 with the net potential energy. QR is based on the decomposition outlined in Sec. II B 1, thus the Boltzmann weight is given by the integrand in Eq. (14) times $\exp(-\beta V_{\rm I}/P)$ with the definition of $V_{\rm I}$ introduced in Eq. (4). HOA is similar to PA, but the term V_1 that appears in $V_{\rm cor}$ is the net potential. QR-HOA is similar to QR, however, the term V_1 that appears in $V_{\rm cor}$ is now $V_{\rm I}$. Thus, mathematically speaking, the underlying decompositions in the various treatments are:

- PA: $\rho_{\rm PA} = \exp(-\beta\hat{T}_{\rm kin}/P)\ \exp[-\beta(V_{\rm harm}+V_{\rm I})/P]$
- QR: $\rho_{\rm QR} = \exp[-\beta(\hat{T}_{\rm kin}+V_{\rm harm})/P]\ \exp(-\beta V_{\rm I}/P)$
- HOA: $\rho_{\rm HOA} = \rho_{\rm PA}\exp(-\beta V_{\rm cor}/P);\ V_1 = V_{\rm harm}+V_{\rm I}$
- QR-HOA: $\rho_{\rm QR-HOA} = \rho_{\rm QR}\exp(-\beta V_{\rm cor}/P);\ V_1 = V_{\rm I}$

Fig. 1 shows the relative error of the energy for the Frenkel Kontorova model at $T = 0.2\ V_0$, $K = 2\ V_0/b^2$, and $m = 0.1\hbar^2/(V_0 b^2)$). In all calculations, we subtracted the classical ground state energy. The convergence is found to be $1/P^4$ with the HOA and the QR-HOA algorithm, while the convergence rate is only $1/P^2$ for PA and QR. The prefactors of the errors are distinctly reduced due to the QR decomposition. In all approaches it is necessary to increase P linearly with inverse temperature, in order to maintain the accuracy of the calculation.

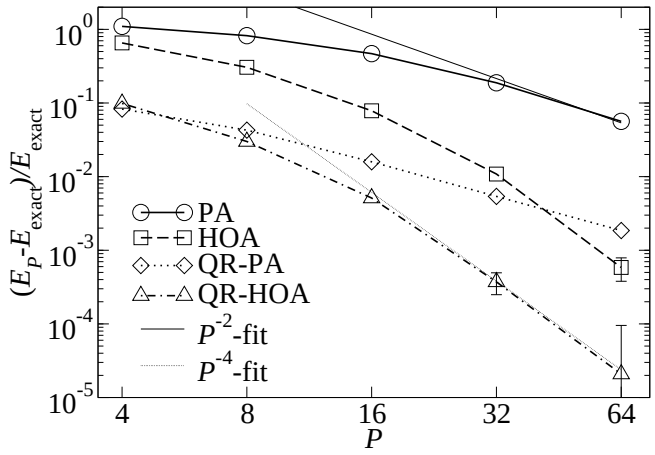

FIG. 1: Relative error of the net internal energy U of the FK model due to the use of finite Trotter numbers P in the four different algorithms examined. Parameters are defined in the text.

The present graph shows that for the given set of parameters, one can achieve 90% accuracy with $P = 4$ if the simulation is based on HOA-QR, while for the same accuracy $P = 64$ is required in the primitive algorithm. For a small systematic error in the order of 10^{-5}, it is sufficient to use $P = 64$ with HOA-QR, while one would need approximatively $P = 6400$ if one wanted to have the same accuracy with the conventionally used primitive approach. The additional calculations that one needs to do in HOA-QR with respect to PA are relatively inexpensive. For instance, one HOA-QR time step for a system consisting of 1,024 particles and $P = 1,024$ requires only twice as much CPU time as a simple PA time step, mainly due to the calculation of $V_{\rm cor}$. Of course, the improvement achieved due to the QR technique depends on the accuracy of the harmonic approximation. For large values of V_0, i.e., in the pinned phase, it is useful to include the harmonic part of the substrate potential in $V_{\rm harm}$ and choose for the rest $V_{\rm I} = -V_0\sum_{j=0}^{N-1}\left(\cos(x_j/b) - 1/2(\delta x_j/b)^2\right)$ with δx_j the deviation between particle's j present position and its mechanical equilibrium position $x_{{\rm eq},j}$, which can be chosen to be $x_{{\rm eq},j} = j2\pi b$.

3. Avoiding critical slowing down

The main task of a path integral simulation program is to sample configurations $\{u_k^\Omega\}$ in such a way that they are distributed according to the weight function W

$$W \propto \exp\left(-\beta V_{\rm eff}/P\right), \tag{23}$$

where $V_{\rm eff}$ is an effective potential that depends on the decomposition discussed above, i.e., for the QR-HOA approach the effective potential would be:

$$V_{\rm eff}^{\rm QR-HOA} = \frac{1}{2}\sum_{k,\Omega}\tilde{\kappa}(k,\Omega) \mid u_k^\Omega \mid^2 + \sum_{\tau=0}^{N-1} V_{\rm I}(\{x_j\}^\tau) + \frac{\hbar^2\beta^2}{12mP^2}\sum_{j,\tau}\left|\frac{\partial V_{\rm I}(\{x_j\}^\tau)}{\partial x_j^\tau}\right|^2, \quad (24)$$

where the set of coordinate u_k^Ω and the set of coordinates x_j^τ are not independent but related via a Fourier transform. Once configurations are visited according to the weight function, thermodynamic averages of observables can be calculated as averages of their estimators, see also Sec. II C.

The sampling is efficient when the correlation time of the observables is small, i.e., when stochastic fluctuations of the estimators decay quickly with time. If no precautions are taken, path integral simulations can suffer from serious ergodicity problem, in particular when P becomes large. Straightforward Monte Carlo methods (moving only individual beads and center-of-masses) as well as straightforward molecular dynamics (every bead gets assigned the same inertia) result in critical slowing down, i.e., the correlation time of the slowest mode increases with P^2. In path integral Monte Carlo (PIMC), this problem can be overcome with staging algorithms, in which a fraction of the chain is moved at once, see Ref. 30 for more details.

In PIMD, a similar speed-up can be obtained by defining appropriate 'dynamical' kinetic energies $T_{\rm dyn}$ [20]. Note that one has a lot of freedom to chose the $T_{\rm dyn}$, because the sampling weight W in the path-integral representation only depends on coordinates. It is desirable to collapse the time scales as much as possible, because in that case, the ratio of the allowed time step Δt to the maximum period T can be chosen relatively large for every mode. One possibility to achieve this as well as possible is to assign inertia (or 'dynamic' masses) to the eigenmodes of a chain such that the intrinsic time scales overlap as much as possible [27]. In their original paper, Tuckerman *et al.* [20] showed that this can also be done by introducing a staging transformation, which reduces the slowing-down with increasing P just as well as assigning masses to eigenmodes.

In our present approach, we may go even further and assign dynamic masses m_k^Ω to the (spatially delocalized) eigenmodes of the unperturbed Hamiltonian. Alternatively, a properly-defined staging transformation may reduce the slowing down also in spatially delocalized harmonic variables. Following the suggestion in Ref. 27 and extending them to the sine Gordon model, a collapse can be done within the harmonic approximation with the following choice [27]:

$$m_k^\Omega = m_k\,\frac{k_{{\rm E},k}+\tilde{\kappa}(k,\Omega)}{k_{{\rm E},k}}, \quad (25)$$

where $k_{{\rm E},k}$ is the classical stiffness of eigenmode k. Note that one leaves the inertia of the center-of-mass mode of the whole system u_0^0 invariant with this choice of m_k^Ω. Further optimization of the masses m_k^Ω can be achieved during the equilibration of the simulation or with the help of a short test run. This is particularly useful when the physical masses are small, because the harmonic approximation becomes invalid. Of course, the additional optimization of the dynamic m_k^Ω can be automated. In either case, the PIMD equation of motion then reads

$$m_k^\Omega \ddot{u}_k^\Omega = -\nabla_{u_k^\Omega} V_{\rm eff}^{\rm QR-HOA} + F_{\rm thermostat}, \quad (26)$$

where $F_{\rm thermostat}$ is the coupling to a thermostat making sure that thermal equilibrium is obtained. We employed a Langevin thermostat and will comment on it further below. In the QR-HOA algorithm, the coefficients $k_{{\rm E},k}$ are related to the curvature of the potential $V_{\rm I}$, which is not yet incorporated in the propagator ρ_Q, thus $k_{{\rm E},k}^{\rm QR-HOA} = V_0/b^2$.

Of course, the dynamics have to be chosen according to and will depend on the nature of the decomposition. Luckily, the higher-order schemes do not require a separate treatment for efficient sampling, because the correction potential $V_{\rm cor}$ vanishes with $1/P^2$ as P increases. Conversely, it does matter whether or not the harmonic part is diagonalized. However, it is straightforward how to assign the values for $k_{{\rm E},k}$ and the dynamical masses. For instance, if we simply did the primitive decomposition of the density matrix, then $\tilde{\kappa}$ would have to be replaced with: [27]

$$\tilde{\kappa}_{\rm PA}(\Omega) = 4\frac{\hbar^2P^2}{m\beta^2}\sin^2(\pi\Omega/P), \quad (27)$$

and the expected local curvature of the potential defined in Eq. (1) would be

$$k_{\rm PA,\,E} = 2K + V_0/b^2. \quad (28)$$

The factor of two on the r.h.s. of Eq. (28) arises from the elastic coupling of an atom to its two neighbors in the FK chain.

Fig. 2 compares the density of states for the centroids in the optimized case (either based on the harmonic approximation or on further automatic optimization) and the physical masses of the centroids. In that figure, we collapsed the data on a frequency close to the Debye frequency of the classical, free chain rather than to the smallest frequency of the system. Also, the internal modes were optimized, i.e., they moved on the same time scale as the fastest centroids. The characteristic dynamics resulting from the 'harmonic' and/or the automatically optimized masses collapse almost perfectly and thus make efficient sampling of the centroids possible. This advantage becomes particularly important when the gap in the dispersion relation vanishes, i.e., in the vicinity of the critical mass. In that region, the 'hydrodynamic slow-down' in the correlation times will be in the order

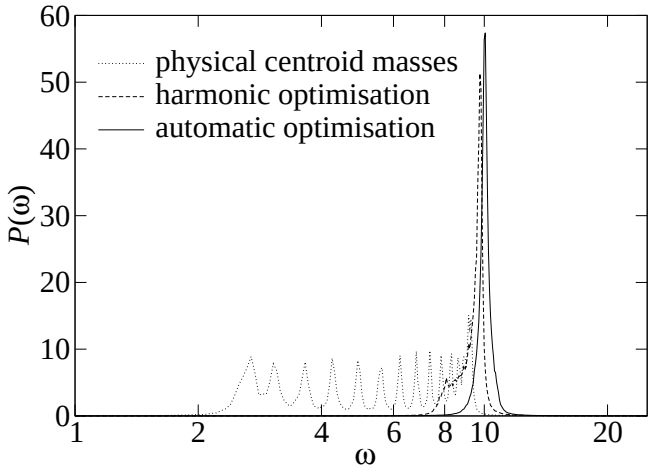

FIG. 2: Centroid density of states for the discrete sine-Gordon chain. The dotted line shows the density of states, calculated with real physical values for the dynamical masses belonging to the u_k^0 coordinates. The dashed line shows the result of the optimization according to Eq. (25). The straight line is the result of an automatic optimization. In all cases, internal modes moved on the same time scale as the fastest centroid mode. Parameters are defined in Sec. II B 2.

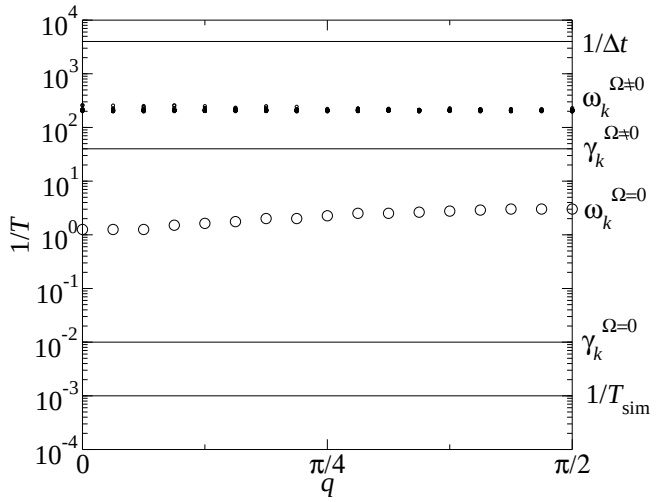

FIG. 3: Realization of the inequalities given in Eq. (29) for $K = 0.1$ and $m = 0.06$.

of N^2, and thus the benefit of artificial masses becomes orders of magnitudes larger than the one shown here. A similar speed-up would not be possible with PIMC techniques, where eigenmode moves turned out less beneficial than in PIMD. Generalized staging moves that incorporate for instance the exact solution of the continuum approximation could be derived and increase the benefit of PIMC. However, such 'sine Gordon staging moves' would be distinctly harder to implement than the regular staging moves, while the implementation of the eigenmode dynamics in PIMD only requires fast Fourier transforms. The PIMD advantage of dating up all modes in parallel is fully bourne out for the sine Gordon model. This advantage is particularly helpful for the calculation of static properties.

We will conclude this subsection by commenting on the thermostat and adiabatic PIMD (aPIMD). In aPIMD, it is necessary to assign the *physical* mass to each center-of-mass mode $u_j^{\Omega=0}$, where j enumerates the atoms and Ω is the frequency conjugate to the imaginary time, i.e., the Matsubara frequency. This translates into $m_k^{\Omega=0} = m$. The internal modes have to move on much smaller time scales, so that they can explore the relevant phase space sufficiently while the centroid moves only a small distance in real space. This can be achieved by dividing the masses m_k^Ω in Eq. (25) by a large number. At the same time, the time step Δt has to be reduced and the coupling to the thermostat increased accordingly. If γ_k^Ω denotes the inverse time constant with which a mode k, Ω is coupled to the thermostat (or alternatively γ_k/ω the number of independent configurations obtained in Monte Carlo, provided the mean forces on the centroids were evaluated in terms of PIMC), then the following series of inequalities should be obeyed

$$\begin{aligned} \Delta t^{-1} &\gg \omega_k^{\Omega\neq 0} > \gamma_k^{\Omega\neq 0} \gg \omega_{k=0}^{\Omega=0}, ..., \omega_{k=\pm\pi b/2}^{\Omega=0} \\ &\gg \gamma_k^{\Omega=0} \gg T_{\rm sim}^{-1}, \end{aligned} \tag{29}$$

where $T_{\rm sim}$ is the time over which trajectories are averaged. Fig. II B 3 shows in how far the inequalities stated in Eq. (29) were satisfied for the calculation of a generic centroid spectrum.

While concerns about Langevin thermostats are not alien to the authors, we have to emphasize that our Langevin implementation, which is described in Ref. 27, including the data presented in Fig. 1 were obtained using that thermostat. Our results remained unaltered within the statistical error bar, which was smaller than the systematic errors, when time step and coupling strength to the thermostat were altered. As a rule of thumb, we take a time step Δt, which is about 4% of the characteristic/minimum period and a damping term $\gamma = 0.01\ \Delta t^{-1}$. For aPIMD simulations, we change from 5'th order Gear predictor corrector to velocity Verlet. The time scale of the internal modes is adjusted to be more than ten times faster than the fastest centroid mode and the thermostat is coupled much less strongly to the centroids than in regular PIMD simulations. Some runs were repeated with a more rigorous integration scheme suggested recently by Ricci and Ciccotti [31]. It turned out that our parameters were chosen carefully enough such that none of the plots had to be changed in a manner that would have been noticeable to the eye. For stronger damping, however, the Ricci-Ciccotti integration scheme is more than likely to prove beneficial.

To summarize the algorithm, coordinates are propagated in reciprocal space, i.e., the variables u_k^Ω are the molecular dynamics variables. Once a new set of u_k^Ω's is obtained, we transform the u_k^Ω's into real space u_j^τ and

calculate the forces due to the non-harmonic forces $F^{\tau}_{\mathrm{I},j}$ in real space. The (inverse) Fourier transform of these forces is added to the diagonal terms. As just noted, the thermostat acts on the u^{Ω}_k's, so that the characteristic relaxation time can be made similar for all internal modes.

C. Estimators

The estimators for the calculation of observables depend on the chosen decomposition. They can be determined from the corresponding thermodynamic expressions for the averages. For the kinetic energy, the potential energy of the harmonic coupling, and an arbitrary operator L diagonal in real space, these expressions read:

$$\begin{aligned} < T > &= \frac{m}{\beta}\frac{d}{dm}\ln\left(Z(\beta,m,W,V_{\mathrm{I}})\right) \qquad (30)\\ < V_{\mathrm{harm}} > &= -\frac{1}{\beta}\,\frac{d}{d\lambda}\ln\left(Z(\beta,m,\lambda W,V_{\mathrm{I}})\right)\Big|_{\lambda=1}\\ < L > &= -\frac{1}{\beta}\,\frac{d}{d\lambda}\ln\left(Z(\beta,m,W,V_{\mathrm{I}}+\lambda L)\right)\Big|_{\lambda=0}. \end{aligned}$$

The estimator for the kinetic energy is given by:

$$\begin{aligned} T^{\mathrm{QR-HOA}}_{\mathrm{est}}\left(\{u^{\Omega}_k\}\right) &= \frac{PN}{2\beta}+\frac{P}{4\beta}\sum_{k=0}^{N-1}\left[\frac{f_k}{\tanh[f_k]}-1\right]\\ &+\frac{1}{P}\Bigg[\sum_{\Omega=0}^{P-1}\sum_{k=0}^{N-1}\frac{1}{2}\Bigg(-\frac{4P}{\sigma_k^2\beta}\sin^2(\pi\Omega/P)\\ &\qquad+\left[\frac{d}{df_k}\tilde{\kappa}(k,\Omega)\right]\frac{f_k}{2}\Bigg)\left(u^{\Omega}_k\right)^2\\ &+V_{\mathrm{cor}}\left(\{u^{\Omega}_k\}\right)\Bigg]. \qquad (31) \end{aligned}$$

The kinetic energy can also be calculated with a virial estimator which shows a well behaved statistical variance in the $P\to\infty$ limit[30, 32]. The virial estimator can be derived by performing a variable transformation of the coordinates $\{u^{\Omega}_k,\ \Omega\neq 0\}$ in the QR-HOA expression for the partition function into the dimensionless variables $v^{\Omega}_k = u^{\Omega}_k/\sigma_k$, performing the derivative according to Eq. (30) and transforming back to the variables u^{Ω}_k. We made sure to incorporate the central mode in the estimator, which is missing in the original formulation of the virial estimator [32]. Doing this is important when a significant number of unbound states contributes significantly to the partition function [30]. The resulting virial estimator in the QR-HOA scheme reads:

$$\begin{aligned} T^{\mathrm{QR-HOA(vir)}}_{\mathrm{est}}\left(\{u^{\Omega}_k\}\right) &= \frac{N}{2\beta}+\frac{1}{4\beta}\sum_{k=0}^{N-1}\left[\frac{f_k}{\tanh[f_k]}-1\right]\\ &+\frac{1}{P}\left[\sum_{\Omega=1}^{P-1}\sum_{k=0}^{N-1}\left(\frac{1}{2}-\frac{1}{4}\left[\frac{f_k}{\tanh[f_k]}-1\right]\right)\times\right.\\ &\times u^{\Omega}_k\frac{d}{du^{\Omega}_k}\left[V_{\mathrm{harm}}\left(\{u^{\Omega}_k\}\right)+V_{\mathrm{I}}\left(\{u^{\Omega}_k\}\right)+V_{\mathrm{cor}}\left(\{u^{\Omega}_k\}\right)\right]\\ &\left.+V_{\mathrm{cor}}\left(\{u^{\Omega}_k\}\right)\right]. \qquad (32) \end{aligned}$$

Here $V_{\#}\left(\{u^{\Omega}_k\}\right)$ $(\#=\{\mathrm{harm},\ \mathrm{I},\ \mathrm{cor}\})$ stands for

$$V_{\#}\left(\{u^{\Omega}_k\}\right)=\sum_{\tau=0}^{P-1}V_{\#}(\{x_j\}^{\tau})\Big|_{x^{\tau}_j=x^{\tau}_j(\{u^{\Omega}_k\})}. \qquad (33)$$

The estimator for the harmonic interaction is given by:

$$\begin{aligned} V^{\mathrm{QV-HOA}}_{\mathrm{harm\ est}}\left(\{u^{\Omega}_k\}\right) &= \frac{P}{4\beta}\sum_{k=0}^{N-1}\left[\frac{f_k}{\tanh[f_k]}-1\right]\\ &+\frac{1}{P}\sum_{\Omega=0}^{P-1}\sum_{k=0}^{N-1}\frac{1}{2}\left(\kappa_k+\left[\frac{d}{df_k}\tilde{\kappa}(k,\Omega)\right]\frac{f_k}{2}\right)\left(u^{\Omega}_k\right)^2 \qquad (34) \end{aligned}$$

The estimator for operator L is

$$\begin{aligned} L^{\mathrm{QV-HOA}}_{\mathrm{est}}\left(\{u^{\Omega}_k\}\right) &= \frac{1}{P}\sum_{\Omega=0}^{P-1}\Bigg[L\left(\{u^{\Omega}_k\}\right) \qquad (35)\\ &+\frac{\hbar^2\beta^2}{24mP^2}\sum_{k=0}^{N-1}\left(\frac{d}{du^{\Omega}_k}V_{\mathrm{I}}\left(\{u^{\Omega}_k\}\right)\right)\left(\frac{d}{du^{\Omega}_k}L\left(\{u^{\Omega}_k\}\right)\right)\Bigg]. \end{aligned}$$

Here $L\left(\{u^{\Omega}_k\}\right)$ is defined through $L\left(\{x_j\}\right)$ in analogy to Eq.(33). Note that the harmonic energy can also be calculated with Eq.(35) setting $L=V_{\mathrm{harm}}$, but the systematic error due to the decomposition would be bigger. The estimator for the internal energy $U=\langle T+V_{\mathrm{harm}}+V_{\mathrm{I}}\rangle$ can be found if one uses $L=V_{\mathrm{I}}$ in Eq.(35).

III. SIMULATION RESULTS

A. Dispersion relation

The phonon dispersion relation $\omega(q)$ is always a quantity of particular interest. To the authors' knowledge, it is only known exactly for the continuum model [24, 33]. In this section, we will discuss $\omega(q)$ for the *discrete* FK model as well as the spectra from which the $\omega(q)$'s for different masses are obtained.

Classically, the zero-temperature dispersion relation of the chain is simply given by

$$\omega^2_{\mathrm{cla}}(q)=\frac{1}{m}\left[4K\sin^2(qb/2)+K_0\right], \qquad (36)$$

where q denotes the phonon's wave number and $K_0=1$. Eq. (36) can be found by a simple harmonic approximation of the sinusoidal embedding potential V_{I} around the minima. The continuum solution of the QFK has the same functional dependence, however, the value of the

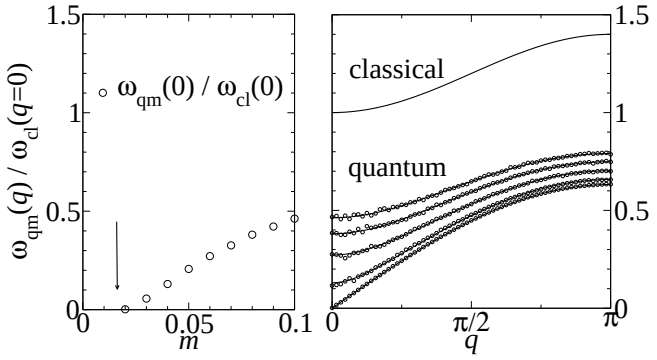

FIG. 4: Right: Dispersion relations for the discrete QFK chain with $K = 0.1$ for different masses, namely $m = 0.02, 0.04, 0.06, 0.08, 0.1$ (from bottom to top) as well as for the classical FK chain (very top curve). Lines are fits according to Eq. (37). Left: Values for effective substrate curvature $\tilde{K}_0$ as a function of mass m, as obtained from the fit for the band gap at zero wave vector. The error indicates the critical mass in the continuum model. All plots were obtained for system size $N = 128$, temperature $T = 0.064$ and the same time-scale separation as in Fig. II B 3.

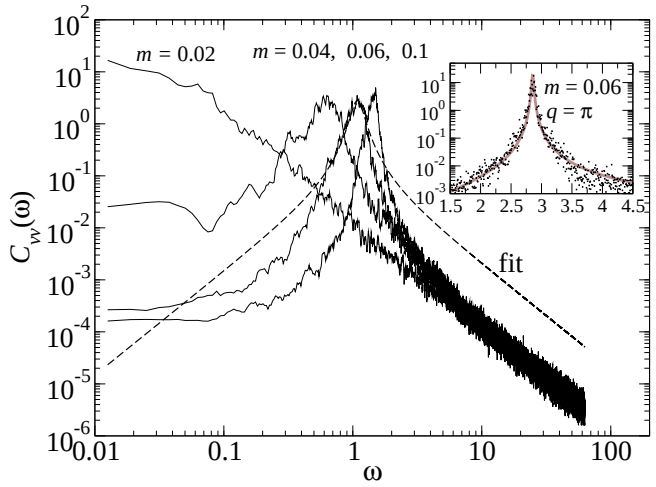

FIG. 5: Spectra reflecting the velocity correlation function of the centroid for different values of m at wavenumber $q = 0$ (main figure) and $q = \pi$ (inset); system size $N = 128$, temperature $T = 0.064$. The dashed line (main figure) and the gray line (inset) are fits according to Eq. (38).

substrate curvature K_0 becomes renormalized to a mass-dependent value $\tilde{K}_0$ due to zero-point quantum fluctuations and/or thermal fluctuations [24, 33]. Thus for the continuum SG, one has

$$\omega^2(q) = \frac{1}{m}\left[4\tilde{K}\sin^2(qb/2) + \tilde{K}_0\right] . \qquad (37)$$

In this equation, we have also generalized the value K to $\tilde{K}$, although in the continuum solution $K = \tilde{K}$.

Eq. (37) also proves accurate for the dispersion in the highly discrete FK model, see the right-hand side of Fig. 4, in which the classical zero-temperature dispersion relation corresponding to the limit $m \to \infty$ is plotted for comparison. Each curve requires only two fit parameters, namely the value for $\tilde{K}$ and $\tilde{K}_0$ in Eq. (37). While the effective maximum substrate curvature $\tilde{K}_0$ can be strongly reduced by quantum fluctuations in the phase with gap and vanishes in the gapless phase, the effective elastic coupling $\tilde{K}$ receives only very small corrections due to quantum fluctuations. $\tilde{K}$'s optimum value turned out to differ at most by 5 % from K, which happened when the masses m were slightly above m_c. In this mass regime, confining $\tilde{K}$ to K lead to apparently systematic deviations between fitted and measured $\omega(q)$'s in the order of but smaller than symbol size. The dispersion relation does not change noticeably when particle number N and inverse temperature β (sufficiently small but fixed β/P) are increased. This allows one to conclude that the dispersion relations given in Fig. 4 represent the thermodynamic and zero-temperature limit within the statistical error bars, which are smaller than the used symbols.

The left-hand side of Fig. 4 shows the phonon excitation gap at zero wave vector. The gap size is determined from the fit parameter $\tilde{K}_0$ in Eq. (37), which is fitted to the data for the dispersion relation. The phonon excitation gap apparently becomes zero at a value $m_c \approx 0.02$, as shown in the left-hand side of Fig. 4. This in turn implies that sliding can be induced at arbitrarily small external driving forces for $m \leq 0.02$. As will be shown later, the system creeps in the zero-gap regime when subjected to a small external driving force. The discreteness of the chain alters the value of the mass m_c at which the transition from finite gap (no creep) to zero gap (creep) takes place. The continuum model predicts this transition to occur at $m_c = 0.016$ [34]. This is in close agreement with the value of $m_c = 0.02$ obtained for the discrete model in this work, which is valid for the choice of $K = 0.1$. The discrepancy between continuum and discrete model will decrease further as the spring stiffness within the chain increases as compared to the maximum curvature $K_0 = 1$ of the embedding potential.

All dispersion relations were obtained by analyzing the spectra of the velocity autocorrelation functions of centroids at fixed wave vector q. The eigenfrequencies ω_0 were obtained by fitting the spectra with a Lorentzian, which for the velocity ($v(\omega) = -i\omega x(\omega)$) autocorrelation function reads

$$C_{vv}(\omega, q) \propto \frac{\omega^2}{\{\omega^2 - \omega_0(q)^2\}^2 + \gamma_{\rm eff}^2\omega^2}. \qquad (38)$$

Some representative centroid spectra of collective modes at zero q vectors are shown in Fig. 5. The Lorentzians provide an excellent approximation for modes that are not too close to zero (see the inset) and a reasonably good approximation to the main part of the $q = 0$ peaks. The tails in the observed $q = 0$ spectra have little bearing on the value of the eigenfrequencies $\omega_0(q)$.

We have analyzed in Fig. 6 how finite temperature

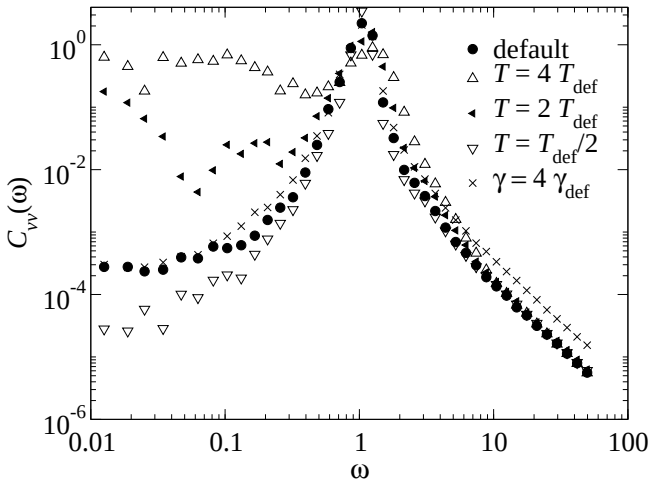

FIG. 6: Similar graph as previous graph, Fig. 5, however, at fixed mass $m = 0.06$ and varying temperature T and damping of central mode γ. The data has been coarse grained such that $\Delta \ln \omega$ is constant at large ω.

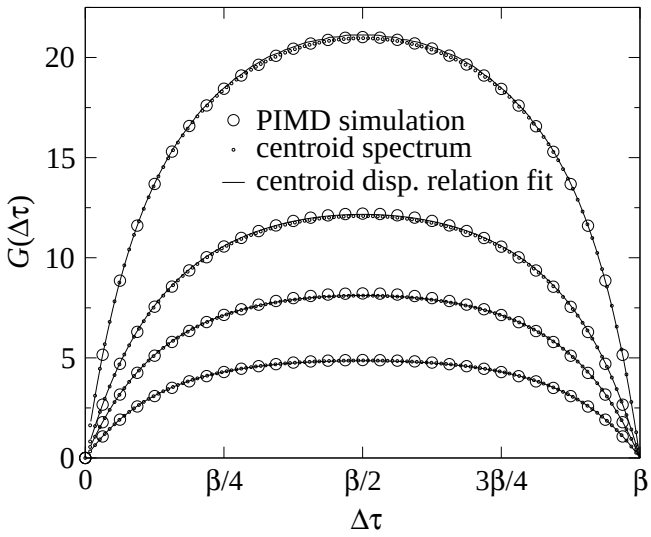

FIG. 7: Single-particle, imaginary-time correlation function $G(\Delta\tau) = \langle [x(\tau + \Delta\tau) - x(\tau)]^2 \rangle$ as obtained by accumulating $G(\Delta\tau)$ directly (open circles) for $T = 0.256$, and as obtained by using the measured single-particle spectra at $T = 0.064$, as well as by using dispersion relations $\omega(q)$ such as those shown in Fig. 11. All simulations were done at $T = 0.256$.

T and finite thermostat γ affect the spectra. Most of this analysis was done for the mass $m = 0.06$ in the pinned regime. At large ω, the spectra show a power law behavior proportional to ω^{-2}. The prefactor of this power law decreases with decreasing γ. For $m = 0.06$, this prefactor scales approximately with $1/\sqrt{\gamma}$. At small ω, we could not identify a systematic trend when γ was changed. Thus the intrinsic damping mechanisms dominate the artificially imposed damping at small ω.

The temperature appears to be mainly responsible for the finite values of $C_{vv}(\omega)$ at small ω in the pinned regime. Reducing the temperature further leads to a decrease in the plateau value of $C_{vv}(\omega)$ at small ω. For $m = 0.06$, our analysis suggests that the zero-temperature limit of $C_{vv}(\omega)$ is zero (or at least extremely small) for frequencies below $\omega_{\min}(m = 0.06) \approx 0.5$. Given the data presented for the $m = 0.06$ case in Fig. 6, one can speculate that there would be no intrinsic frequency in the system above a frequency $\omega_{max}(m = 0.06) \approx 3$ if one was able to run 'ideal' simulations in the limit $T \to 0$ and $\gamma \to 0$. Having (significant) intensity only in a small window in the interval $0.5 \leq \omega \leq 3$ shows a distinct deviation from what one would expect from Gaussian noise.

More importantly, the shape of the FK spectra in the pinned regime differs from those of the continuous SG. The latter show an intensity that monotonically increases with decreasing ω until ω_{min} is reached at which point the intensity abruptly drops to zero. In the discrete FK model, there seems to be different universality in that the spectra tends to zero continuously after going through a maximum.

Lastly, we would like to point out an unexpected maximum in our data located at zero frequency for finite temperatures T. This peak can be related to thermal creep of the manifold, rather than to quantum creep, which is the main subject of the following analysis.

B. Consistency of real-time and imaginary-time data

As mentioned in our previous publication on the discrete QFK model [22], there are legitimate concerns [18] about the necessity to introduce corrections to the dynamical interpretation of adiabatic path integral molecular dynamics (aPIMD). In order to check the applicability of the dynamical interpretation of aPIMD for a specific model of interest, it is possible to compare numerically exact imaginary-time correlation functions with those that are reproduced indirectly from the dynamical aPIMD correlation functions. Of course, such a self-consistent check is particularly meaningful if it is done for parameters, where the system is non-classical, correlated, and anharmonic. In the present context, this is the case at small temperatures for particle masses close to the critical mass m_c.

The imaginary-time correlation function $G(\Delta\tau) = \langle [x(\tau + \Delta\tau) - x(\tau)]^2 \rangle$ can be easily monitored in the simulation and it can also be calculated indirectly from spectra such as those presented in Fig. 5. A comparison of the two ways to yield $G(\Delta\tau)$ is shown in Fig. 7. It turns out that the agreement is almost perfect even if $m = m_c$. Thus, except for very fine details in the spectra such as the detailed behavior of tails, one can expect aPIMD to provide the correct behavior.

We would like to mention that for the quantitative agreement displayed in Fig. 7, it is absolutely necessary to

chose very small values of the externally imposed thermostat. For values of γ that are only four times higher than those shown in Fig. 4, the agreement is distinctly less good and obvious gaps open up between directly and indirectly evaluated imaginary time correlation functions. Interestingly, the dispersion relations are much less sensitive to the precise choice of γ than the imaginary-time correlation functions. For the present $G(\tau)$, it is also possible to generate good approximations by using the spectra and giving each 'eigenfrequency' $\omega_j(q)$ simply the weight $\delta(\omega - \omega_j(q))$.

Of course, the true test of aPIMD is the question how well it performs when the observables are mainly sensitive to correlated tunneling. This question will be addressed indirectly when analyzing the different natures of the gapless and the gapped phase.

C. Particle delocalization and tunneling

In the previous paragraphs, it was shown by PIMD that the ground state of the quantum sine-Gordon chain undergoes a phase transition from a phase with a gap to a gapless phase as the mass is decreased below a critical value m_c. The different structures of the two ground states in the two phases were characterized in terms of the phonon dispersion relation (Fig. 4). For a more physical understanding of the processes that lead to this behavior, the gyration radius of the imaginary-time path and the imaginary-time minima correlation function are analyzed in this paragraph. It will be shown that tunneling in imaginary-time is the process that drives the phase transition and that the importance of tunneling with decreasing temperature is qualitatively different in the two phases. The gyration radius R_g can be considered as a measure for the quantum mechanical delocalization of a particle. It can be defined as

$$R_g^2(T) = \left\langle \left(\hat{x} - e^{-\beta\hat{H}/2}\hat{x}e^{\beta\hat{H}/2} \right)^2 \right\rangle \qquad (39)$$

with $\beta = 1/(k_\mathrm{B}T)$. The temperature dependence of the gyration radius R_g is shown in Fig. 8 for various particle masses. The gyration radii can also be calculated from the centroid spectra directly or for ensembles of harmonic oscillators with the frequencies given by the fit of the centroid dispersion relation (Fig. 4). The agreement between gyration radii calculated from the centroid dispersion relations, the centroid spectra and the results stemming from the PIMD simulation is good. In the phase with the gap where $\tilde{K}_0 > 0$, the gyration radius R_g levels at a finite value as the temperature is decreased, while in the gapless phase with $\tilde{K}_0 = 0$ the gyration radius diverges logarithmically with $\beta = 1/k_\mathrm{B}T$. This means that in the gapless phase the delocalization of a particle becomes increasingly important with decreasing temperature, while a particle's delocalization remains finite in the phase with the gap as the temperature goes to zero.

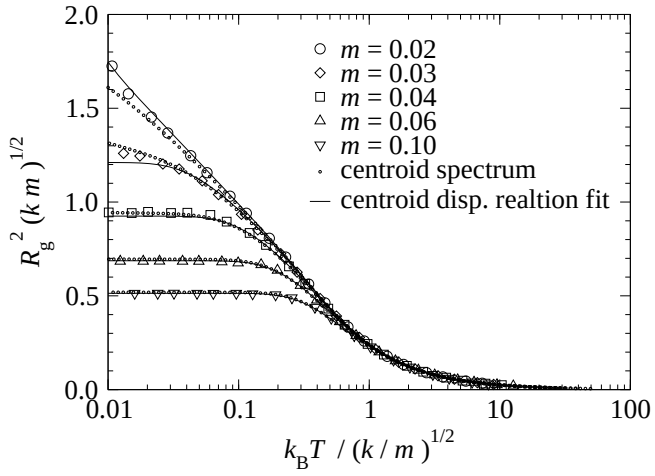

FIG. 8: Temperature dependence of the single-particle gyration radius. The symbols are the results from a PIMD simulation and the lines correspond to harmonic ensembles given by the centroid dispersion relations. The dotted lines are the gyration radii calculated directly form the centroid spectra at $T = 0.064$ from which the dispersion relations are found as well.

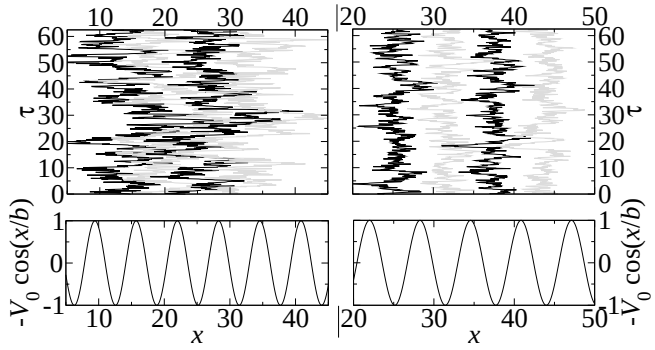

FIG. 9: Above: Imaginary-time trajectories of typical configurations, left: m = 0.02, right m = 0.1, calculated with $T = 0.016$, $N = 128$ and $P = 512$. Below: substrate potential

Another quantity which can characterize the structure of the different discrete quantum sine-Gordon chain's ground states can be found if one observes the importance of the tunneling process in imaginary time. Fig. 9 shows typical imaginary-time trajectories at different masses, i.e., one for $m = 0.02$ in the gapless region and the other one for $m = 0.1$ in the phase with a gap. While the particles are mainly located near one minimum in the phase with the gap, particles are delocalized over various minima in the gapless phase. For a more qualitative understanding of the importance of the tunneling process, the imaginary-time minima correlation function $\langle s(0)s(\tau)\rangle$ is considered. Here the function $s(x)$ can be either $+1$ or -1 and it changes its sign between neighbored minima. The behavior of the correlation function $\langle s(0)s(\tau)\rangle$ is a mea-

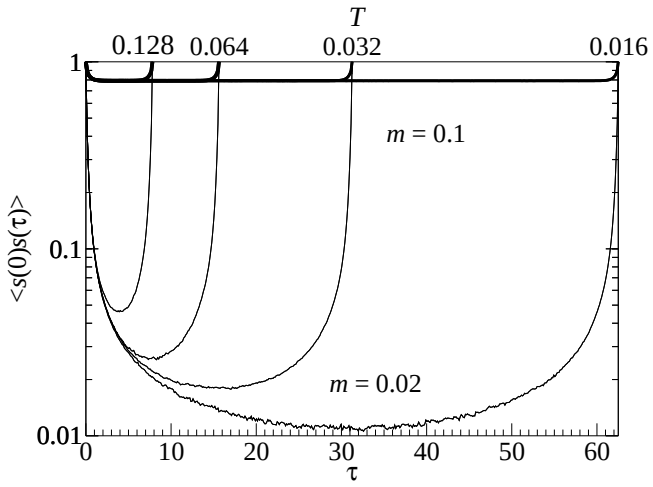

FIG. 10: The imaginary-time minima correlation function in the phase with and without gap. In the phase with a gap ($m = 0.1$) the correlation function levels to a finite value as the temperature is decreased, while in the gapless phase the correlation function decays to zero.

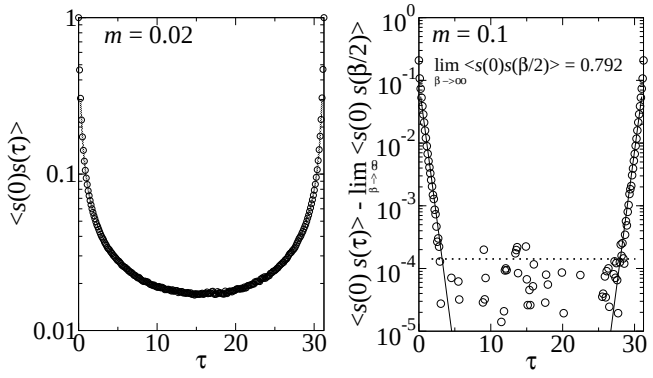

FIG. 11: Left: Algebraic fit of the minima correlation function for $m = 0.02$ with $\kappa = 0.085$ according to Eq. (41). Right: Exponential fit of the minima correlation function for $m = 0.1$ with $\tau_0 = 2.0$ according to Eq. (40). Note that the constant $\lim_{\beta\to\infty}\langle s(0)s(\beta/2)\rangle = 0.792$ is subtracted from the original correlation function. The dotted line indicates the magnitude of the statistical noise.

sure for the importance of tunneling along the imaginary-time axis. For $\tau = 0$, the minima correlation function is always unity by construction. If tunneling never occurs, $\langle s(0)s(\tau)\rangle$ would remain constantly unity along the imaginary-time axis. Fig. 10 shows the imaginary-time minima correlation functions for different temperatures and particle masses $m = 0.1$ and 0.02. The system size is chosen such that finite size effects are smaller then the line thickness. For the higher temperatures a system size of $N = 64$ particles turned out to be sufficient while below $T = 0.032$ $N = 128$ was used. As shown in Fig. 11, $\langle s(0)s(\tau)\rangle$ decays exponentially to finite values in the phase with the gap ($m = 0.1$ is shown exemplarily). The minima correlation function can be fitted well with the functional form:

$$\langle s(0)s(\tau)\rangle \propto C + \left\{ \exp\left(\frac{-\tau}{\tau_0}\right) + \exp\left(\frac{+\tau - \hbar\beta}{\tau_0}\right)\right\} , \tag{40}$$

where C turns out to be positive and finite. Hence, each particle is located mainly in one minimum of the substrate potential. In contrast to that, $\langle s(0)s(\tau)\rangle$ decreases algebraically in the gapless phase with the power law:

$$\langle s(0)s(\tau)\rangle \propto \left[\left(\frac{\tau}{\hbar\beta}\right)^{-\kappa} + \left(1 - \frac{\tau}{\hbar\beta}\right)^{-\kappa}\right] . \tag{41}$$

Within the accuracy of the simulation there was no evidence of a finite offset in Eq. (41) to which $\langle s(0)s(\tau)\rangle$ converges as $\tau \to \infty$ and $\beta = 2\tau/\hbar$. The different behavior of the correlation function in the two phases is in accordance with the predictions for the continuum model [35].

D. Mobility of the discrete QFK chain

In the phase with finite gap at $q = 0$, the continuous QSG model is said to have a mobility that obeys an Arrhenius like behavior [8] and the corresponding energy barrier ΔE is predicted to be proportional to the gap, while in the gapless phase the mobility remains finite down to absolute zero. We have commented briefly on the mobility in our previous work on the discrete QFK model [22] and wish to present in addition some of the details of those results. While the mobility elastic manifolds is finite at finite T [36], it is important to keep in mind that the energy barriers ΔE can be strongly reduced with respect to the classical limit due to quantum fluctuations.

In the following few calculations, the mobility or the resulting diffusion coefficient D will be obtained from the fluctuations of the centroids u_0 at wavenumber $q = 0$, which we define as

$$u_0 = \frac{1}{P\sqrt{N}} \sum_{j=0}^{N-1} \sum_{\tau=0}^{P-1} x_j^\tau . \tag{42}$$

The choice of the normalization factor $1/\sqrt{N}$ eliminates trivial size dependence for the mean-square displacement (MSD) in the pinned and in the unpinned regime, see, for instance, Fig. 1 and Fig. 10 in Ref. 37, where a similar mobility analysis was carried out for two elastically deformable three-dimensional solids in contact. Some representative MSD curves for the gapped phase in the QFK model are shown exemplarily for $m = 0.1$ at various T in Fig. 12. Remember that the system with $m = 0.1$ shows an excitation gap at zero temperature and is hence pinned at $T = 0$. Variation of the number of particles N in Fig. 12 confirmed that finite size effects are much smaller than the statistical errors for systems with $N = 32$ or more particles.

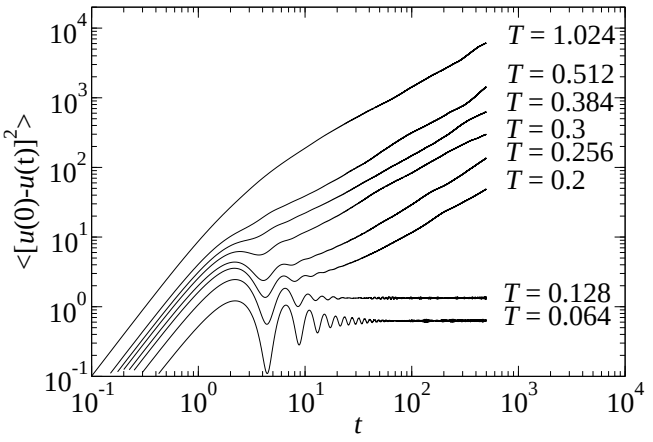

FIG. 12: Mean square displacement of the collective central mode in the phase with a gap ($m = 0.1$, $N = 32$)

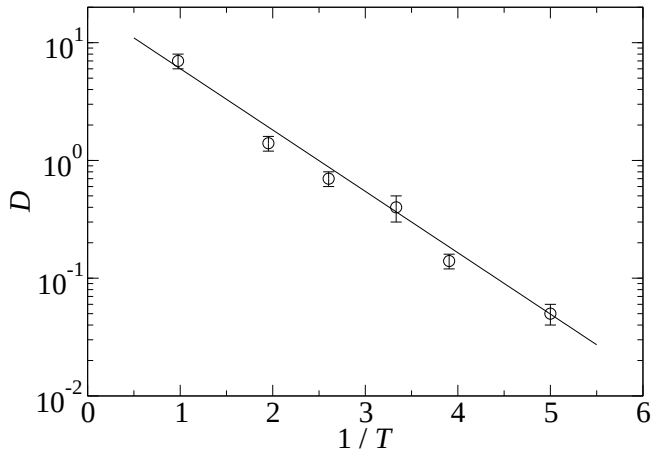

FIG. 13: Arrhenius plot of the diffusion constant determined from the mean square displacements shown in Fig. 12.

In the calculations for the MSD, we have reduced the coupling of the centroid to the external thermostat $\gamma_k^{\Omega=0}$ by a factor of four, in order to minimize an artificial suppression of the chain's mobility. Of course, one cannot give up an external thermostat altogether, in particular when being in the gapless phase. If the thermostat was absent, even a small externally applied force would accelerate the chain to infinitely large velocities. This would not reflect a physically meaningful response, since some energy would always be dissipated into the substrate's phonon bath. Hence, in the gapless phase (or whenever a large external force is applied), the response of the chain will be sensitive to the coupling of the chain to the substrate's phonon bath.

For the same calculations, the damping of the internal modes was altered as well. The damping of the internal modes $\gamma_k^{\Omega\neq 0}$ was increased until convergence of the data was achieved. In this procedure, the eigenfrequencies $\omega_k^{\Omega\neq 0}$ were always adjusted through the choice of their associated 'dynamical' masses $m_k^{\Omega\neq 0}$ such that the internal vibrations were not yet underdamped, namely $\omega^{\Omega\neq 0}/\gamma^{\Omega\neq 0} = 4$. This allowed for an efficient sampling of the internal modes and provided a good approximation to have the centroids move on the free energy profile provided by the internal modes.

Diffusion constants were obtained by analyzing the mean-square displacements of the chain's centroid, Of course, the chain appears to be pinned during the time of the simulation at small T, while at large T, the chains are quite mobile, i.e., it crosses over from the ballistic to the diffusive regime without passing through an intermittent subdiffusive regime. From curves such as in Fig. 12, it is possible to extract diffusion coefficients, i.e., by fitting the slope of $\langle [u(q=0,0) - u(q=0,t)]^2 \rangle$ with respect to t at large values of t. Thus, with the present definition of the centroid (which needs another division by $\sqrt{N}$ to be the true center of mass, one can obtain for the centroid's effective diffusion constant $D_c = N D_N$ (D_N being the size-dependent diffusion constant)

$$D_c = \frac{1}{2} \lim_{t' \to \infty} \left[\partial_t \left\langle \{u(t) - u(0)\}^2 \right\rangle \right]_{|t'} \qquad (43)$$

The temperature dependence that is obtained from the just-described procedure is shown in Fig. 13, in which the Arrhenius type behavior is clearly bourne out.

Note that the functional dependence of the centroid's diffusion constant D_c is qualitatively different in the phase with gap than in the gapless phase, i.e.,

$$D_c \propto \begin{cases} \exp(-\Delta E/k_B T) & \text{with gap; } \Delta E > 0 \\ const\ k_B T & \text{gapless} \end{cases} \qquad (44)$$

In order for a highly continuous chain to move in the phase with gap, a kink/anti-kink pair must be created by thermal activation. Once created, the pair still needs to overcome the Peierls-Nabarro barrier, in order to invoke sliding motion. These processes plus corrections from higher-order multi-kink interactions are reflected in the Arrhenius energy ΔE.

E. The driven FK chain

There is considerable interest in the non-linear response of many systems to external forces such as the current-voltage relation of quasi one-dimensional wires or that of one-dimensional charge density waves. As argued in the introduction, both classes of problems are believed to be isomorphic to the SG or to the FK model. In the previous part of this paper, we were mainly concerned with equilibrium properties and equilibrium fluctuations that can be related to linear response functions. Thus, if one is interested in the non-linear regime, which is the subject of this section, one has to go beyond the treatment so far. Calculating higher-order coefficients from equilibrium fluctuations is a slowly converging and

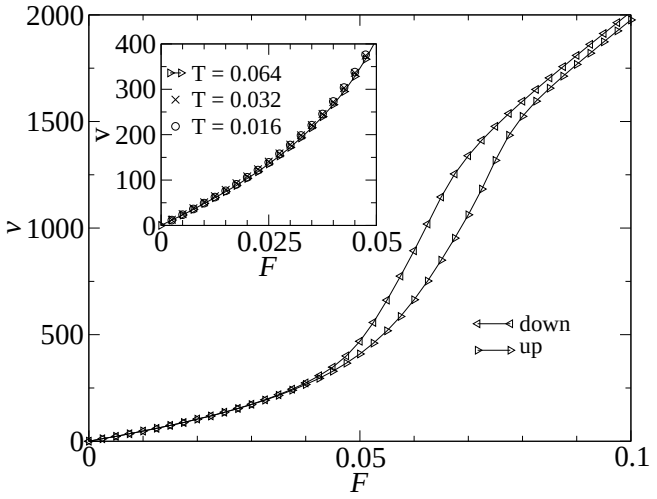

FIG. 14: Center of mass velocity v of a chain as a function of the force F applied on each particle. The simulations start in thermal equilibrium at $F = 0$, the force is then cranked up (triangles pointing to the right) and then reduced (triangles to the left). Details of the simulations are: $m = 0.02$, $T = 0.064$, $N = 32$, and coupling to the thermostat as in Sec. III D.

hence tedious procedure. We will therefore apply external forces directly and measure the current as a function of the external force. The analysis focuses on the small temperature limit, which can be determined by extrapolation from finite T to small T.

To study the response to an externally applied field, a homogeneous force F is applied to each particle by adding a term $-F\sum_{j=0}^{N-1}\hat{x}_j$ to $\hat{H}$. The thermostats coupled to the centroid variables are needed to dissipate the energy pumped into the system by the external driving force F. The Hamiltonian which is considered has the form

$$\hat{H} = \sum_{j=0}^{N-1}\left(\frac{\hat{p}_j^2}{2m}+\frac{1}{2}K(\hat{x}_j-\hat{x}_{j+1})^2 - V_0\cos(\hat{x}_j/b) - F\hat{x}_j\right) + H_{\rm bath} \tag{45}$$

where the bath is modeled as a Langevin equation with a classical fluctuating force and a friction term.

From the results in the previous sections, one may expect zero flow at small external forces in the phase with gap, while the system will show finite flow in the gapless phase proportional to the externally applied force. While (quantum) continuum approximations of the SG model predict damping to vanish at small temperature [7], the (classical) chain's discreteness is known to change this property in classical systems because kink-phonon interactions damp solitons [38, 39]. In Fig. 14, we show the response for a gapless system, namely for $m = 0.02$.

Linear response is found at small velocities in the gapless case. The effective drag coefficient or effective damping term $\gamma_{\rm eff}$ to be defined as

$$\gamma_{\rm eff} = \frac{1}{m}\lim_{F\to 0}\frac{F}{v}\,, \tag{46}$$

has a well-defined finite value, which corresponds to that which is obtained from a fluctuation-dissipation relation

$$\gamma_{\rm eff} = \frac{k_B T}{mD} \tag{47}$$

As can be seen in the inset to Fig. 14, $\gamma_{\rm eff}$ is independent of temperature T at small values of T, which clearly indicates that the motion is not a thermally activated process but due to collective tunneling. This zero-temperature creep motion in the gapless phase is an example for a macroscopic property that is qualitatively changed by quantum fluctuations with respect to the classical system. We may add that at small velocities or small external forces, $\gamma_{\rm eff}$ turns out to be insensitive to the externally imposed γ as long as γ is greater than zero but sufficiently enough smaller than $\gamma_{\rm eff}$. Moreover, a finite size analysis confirms that size effects are not significant for $N \geq 32$ in the creep regime.

At large forces, another linear $v(F)$ regime is observed at forces $F > 0.075$. Here, the damping coefficient $\gamma = F/v$ is the same as the externally imposed one. Thus, the chain moves so quickly over the substrate that internal damping mechanisms are frozen out, i.e., the coupling between solitons and phonons becomes inefficient. In between high and low-velocity regime, the response is not only nonlinear, but a dynamical hysteresis can be observed. While increasing the external force F from below, the chain moves with smaller velocity than if F is reduced from above. This effect can be understood in terms of the non-linear dynamics of the classical Frenkel Kontorova model, i.e., there are different attractors for stable motion. To be specific, the motion at small velocities is dominated by kink motion while the chain becomes 'fluid-like' at high velocities [40]. Coming from small velocities makes the system fall into the attractor with the smaller average velocity, i.e., into the kink motion regime. The details of this dynamical hysteresis depend on γ and are not an intrinsic property of the Frenkel Kontorova model, i.e., the smaller γ the smaller the velocities at which the loop closes.

For masses $m > m_c$, the behavior at medium and large forces is similar to that of $m < m_c$, i.e., there is a 'classical' dynamic hysteresis as can be seen in the main part of Fig. 15. However, a new effect shows up at small-velocity for $m > m_c$, which is shown in the inset of Fig. 15. The new hysteresis is qualitatively different from the one discussed before., Coming from zero external force, the system remains unpinned up to a threshold force of $F^* \approx 0.03$. Above F^*, the system's average velocity v varies linearly with F. Reducing the external force back below F^* results in a secondary hysteresis. This time there is one pinned and one unpinned solution as opposed to the two competing sliding solutions discussed in terms of the classical FK model.

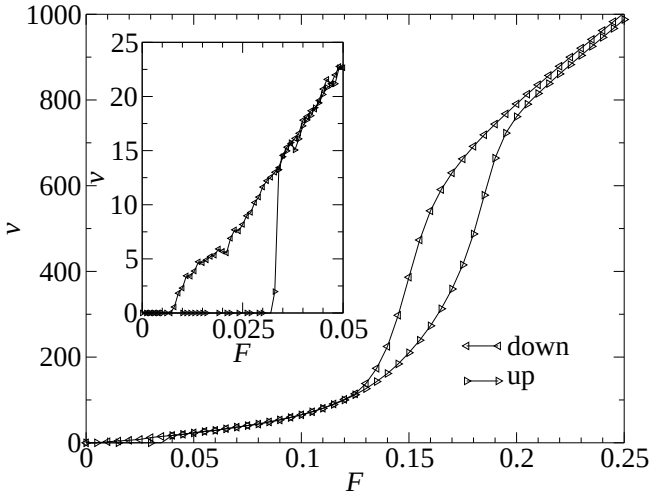

FIG. 15: Same as previous figure but for a mass $m = 0.1$ in the pinned regime; temperature $T = 0.064$ and system size $N = 32$.

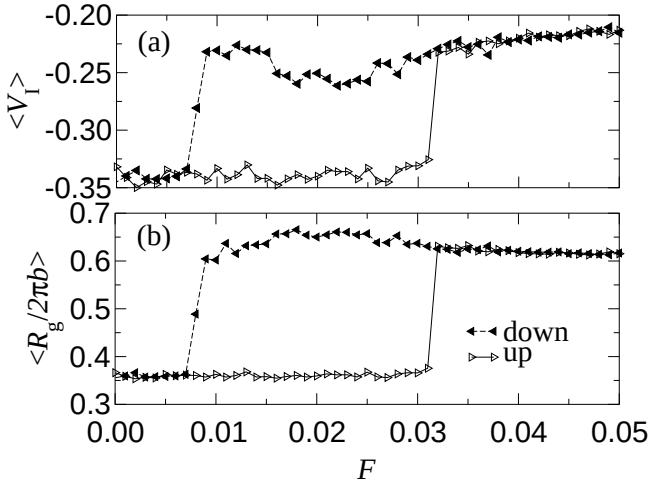

FIG. 16: (a) Average potential energy $\langle V_{\rm pot}\rangle$ and (b) average radius of gyration $\langle R_g\rangle$ as a function of the externally applied force F.

Since sliding at small velocities and zero temperature must be due to quantum fluctuations, one might classify this new effect as a quantum hysteresis. This means that transport in the unpinned regime at small v must mainly be due to tunneling. Indeed, when analyzing average potential energy $\langle V_{\rm pot}\rangle$, and the average radius of gyration R_g, one can associate the pinned state with the one in which the particles are more localized, as is shown in Fig. 16(b) by means of R_g. Hence, one may argue that the kinetic energy is higher in the pinned regime and due to tunneling, smaller in the sliding regime. For the potential energy, shown in Fig. 16(a), the opposite is true.

Of course, so far we have assumed that the limit $T \to 0$ was reasonably well be satisfied for the purposes of our study. However, since our temperature is not exactly zero, there will always be some creep and the pinned regime at small $v(F)$ only appears to be zero within the statistical error bar.

In the phase with a gap, the reaction of the system to an external force at $T = 0$ does not differ qualitatively from the classical system. Fig. 15 shows the force-velocity relation for $m = 0.1$. The system remains pinned until the force reaches a critical value $F_c \approx 0.032$ where the depinning transition occurs.

To conclude, in order to invoke sliding in the extremely discrete FK chain, temperature has to be finite, the external force sufficiently large, or the mass sufficiently small.

IV. CONCLUSIONS

In this study, we presented a detailed analysis of the static and dynamic properties of the commensurate, quantum Frenkel Kontorova (FK) model with a focus on extremely discrete systems, in which the maximum curvature of the embedding potential distinctly exceeds that of the harmonic potentials connecting two particles in the FK chain. In particular, we investigated a regime in which the classical FK chain has many different mechanically stable states, i.e., dislocations are pinned at zero temperature. For such levels of discreteness, results obtained from the continuum solution (which assumes small variations in the phase as a function of particle index) must be asked into doubt. Even in our highly discrete regime, quantum mechanical zero point fluctuations depin the dislocations if the mass of the particles is smaller than a given threshold value m_c.

One of the questions we were interested in was whether adiabatic path integral molecular dynamics (PIMD) is able to provide information on the dynamics of this highly-correlated, many-body quantum system. It turned out that the centroid's time correlation functions, $C_{\rm c}(t)$, are meaningful. In the present case, we successfully reproduced for instance the logarithmic dependence of correlation functions on temperature (or imaginary time), although the centroid's time correlation functions proved highly sensitive to the choice of the externally imposed thermostat. Even though the unpinned, commensurate Frenkel Kontorova chain is only moderately chaotic [40], the observed self consistency is a non-trivial result for various reasons. There have been legitimate claims that the dynamical interpretation of adiabatic PIMD is not rigorous for highly correlated systems [18] and for very non-linear systems [19]. The latter claim is supported by unpublished data by one of us (MHM) on the hydrogen problem in a confining cavity, for which a systematic and significant discrepancy between the exact dipole-dipole correlation functions and adiabatic PIMD data occurs.

Even when the aPIMD correlation functions are not exact, we want to note that reproducing imaginary-time correlation functions from centroid correlation functions

adds new information. The inverse transformation from imaginary-time correlation functions to real time data can yield very accurate results if the centroid spectra are used as a weight function for a maximum entropy fit, as is discussed in detail elsewhere [41]. Thus, being able to reproduce imaginary-time functions from the beginning seems to be supporting evidence for the correctness of adiabatic PIMD on a case to case basis. These self-consistency checks will be particularly important for highly chaotic systems and for those cases in which the second derivative of the anharmonic potential spans a broader range of values than it does in a simple sinusoidal potential.

In order to work with an efficient simulation program, we implemented a propagator in which the leading quantum corrections vanish with $1/P^4$, where P is the Trotter number. Moreover, we avoided critical slowing down by expressing the dynamics in terms of the eigenmodes of the free chain and by attributing masses $m_{q,\Omega}$ to the eigenmodes (characterized by a wavenumber q and a Matsubara frequency Ω) rather than to the individual "beads" or individual ring polymer representing one quantum mechanical point particle. This allowed us to have all the internal modes equilibrate at the same rate, which is necessary in order to have small stochastic error bars and/or to use the centroid interpretation of path integrals in a reliable way.

While some aspects of this study highlighted previously found results [22] in more detail, such as the details of algorithm and implementation of the PIMD code, new results on the discrete, quantum FK chains were presented as well. Our results indicate that the discrete FK chain deviates qualitatively from the continuous sine Gordon (SG) chain in various aspects. In the pinned regime ($m > m_c$), we found that the functional form of the spectrum at zero wave number does not take its maximum value at the cut-off frequency as is the case in the continuum solution [8]. Instead, coming from large frequencies, the spectrum continuously goes to zero after passing through a maximum. In the unpinned regime ($m < m_c$), we find a well-defined and only weakly temperature-dependent drag coefficient, while the quantum SG chain vanishes as an algebraic power law with temperature T as T is decreased [8].

We also identified a dynamical quantum hysteresis at small external forces for masses m above the critical mass m_c, which separates the pinned from the unpinned chain at zero external force. Coming from a pinned state, the chain remained pinned upon increasing the external driving force up to a value F^*, where it depinned. Once the chain was set in motion, decreasing the mass lead to a hysteretic loop. During the sliding motion, the particles were much more strongly delocalized, indicative of a small kinetic energy. At higher forces, a second hysteresis loop shows up, which can be understood in analogy to the classical Frenkel Kontorova model, i.e., there are different dynamical attractors in which the chain can fall depending on the previous history. So far, we have not become aware of an experiment showing this double hysteresis, and in that sense our calculation can be seen as a prediction. For masses above the depinning threshold m_c, we only observe a single hysteresis, which can be understood in terms of the classical Frenkel Kontorova model as different sliding states of the chain, i.e., a (classical) kink-dominated sliding state and a fluid-like state of the chain [40].

Acknowledgments

Support from the National Sciences and Engineering Research Council of Canada (NSERC), SHARCnet, and from the Materialwissenschaftliche Forschungszentrum Rheinland-Pfalz is gratefully acknowledged.

[1] Y. I. Frenkel and T. Kontorova. On the theory of plastic deformation and twinning. *Zh. Eksp. Teor. Fiz.*, 8:1340, 1938.

[2] O. M. Braun and Yu. S. Kivshar. Nonlinear dynamics of the Frenkel-Kontorova model. *Phys. Rep.*, 306:2–108, 1998.

[3] L. M. Floria and J. J. Mazo. Dissipative dynamics of the Frenkel-Kontorova model. *Adv. Phys.*, 45:505–598, 1996.

[4] M. H. Müser, M. Urbakh, and M. O. Robbins. Statistical mechanics of static and low-velocity friction. *Adv. Chem. Phys.*, 126:187–272, 2003.

[5] L. S. Levitov and A. M. Tsvelik. Narrow-gap Luttinger liquid in carbon nanotubes. *Phys. Rev. Lett.*, 90:016401, 2003.

[6] T. Ando and Y. Arakawa, editors. *Mesoscopic Physics and Electronics*. Springer, Berlin, 1998.

[7] X. Zotos and P. Prelovšek. *Physics and chemistry of materials with low dimensional structures*. Kluwer Academic Publishers, Dordrecht, in press, 1999.

[8] T. Giamarchi. Mott transition in one dimension. *Physica B*, 230:975–980, 1997.

[9] E. K. Sklyanin, L. A. Takhtadzhyan, and L. D. Faddeev. Quantum inverse problem method I. *Theor. Math. Phys.*, 40:194, 1979.

[10] B. Hu and B. Li. Ground-state wave function of the quantum Frenkel-Kontorova model. *Europhys. Lett.*, 46:655–660, 1999.

[11] C.-L. Ho and V. C.-I. Chou. Simple variational approach to the quantum Frenkel-Kontorova model. *Phys. Rev. E*, 63:016203, 2001.

[12] F. Borgonovi, I. Guarneri, and D. Shepelyansky. Destruction of classical cantori in the quantum Frenkel-Kontorova model. *Phys. Rev. Lett.*, 63:2010–2012, 1989.

[13] G. P. Berman and E. N. Bulgakov. Coherent structures in the ground-state of the quantum Frenkel-Kontorova model. *Phys. Rev. B*, 49:8212–8226, 1994.

[14] J. V. Alvarez and C. Gros. Conductivity of quantum spin chains: A quantum Monte Carlo approach. *Phys. Rev. B*, 66:094403, 2002.

[15] O. V. Zhirov, G. Casati, and D. L. Shepelyansky. Quantum phase transition in the frenkel-kontorova chain: From pinned instanton glass to sliding phonon gas. *Phys. Rev. E*, 67:056209, 2003.

[16] J. Cao and G.J. Martyna. Adiabatic path integral molecular dynamics methods. II Algorithms. *J. Chem. Phys.*, 104:2028, 1996.

[17] S. Jang and G. A. Voth. Path integral centroid variables and the formulation of their exact real time dynamics. *J. Chem. Phys.*, 111:2357, 1999.

[18] R. Giachetti, R. Maciocco, and V. Tognetti. Effective potential and quantum dynamical correlators. *Phys. Lett. A*, 252:157, 1999.

[19] G. Krilov and B. J. Berne. Real time quantum correlation functions. I. centroid molecular dynamics of anharmonic systems. *J. Chem. Phys.*, 111:9140–9146, 1999.

[20] M. E. Tuckerman, B. J. Berne, G. J. Martyna, and M. L. Klein. Efficient molecular dynamics and hybrid Monte Carlo algorithms for path integrals. *J. Chem. Phys.*, 99:2796, 1993.

[21] J. Cao and G. A. Voth. A new perspective on quantum time correlation functions. *J. Chem. Phys.*, 99:10070, 1993.

[22] F. R. Krajewski and M. H. Müser. Quantum creep and quantum creep transitions in 1D sine-Gordan chains. *Phys. Rev. Lett.*, 92:art.–no. 030601, 2004.

[23] F. R. Krajewski and M. H. Müser. Many-body quantum dynamics by adiabatic path-integral molecular dynamics: Disordered frenkel kontorova models. *Comp. Phys. Comm.*, page submitted.

[24] R. Giachetti and V. Tognetti. Variational approach to quantum statistical mechanics of nonlinear systems with application to sine-Gordon chains. *Phys. Rev. Lett.*, 55:912, 1985.

[25] A. Cuccoli, R. Giachetti, V. Tognetti, R. Vaia, and P. Verrucchi. The effective potential and effective hamiltonian in quantum-statistical mechanics. *J. Phys.: Cond.-Mat*, 7:7891–7938, 1995.

[26] M. Takahashi and M. Imada. Monte-Carlo calculation of quantum-systems. 2. Higher-order correction. *J. Phys. Soc. Jap.*, 53:3765–3769, 1984.

[27] M. H. Müser. On new efficient algorithms for PIMC and PIMD. *Comp. Phys. Comm.*, 147:83, 2002.

[28] H. De Raedt and B. De Raedt. Applications of the generalized trotter formula. *Phys. Rev. A*, 28:3575–3580, 1983.

[29] F. R. Krajewski and M. H. Müser. Comparison of two non-primitive methods for path integral simulations: Higher-order corrections vs. an effective propagator approach. *Phys. Rev. B*, 65:174304, 2002.

[30] D. M. Ceperley. Path integrals in the theory of condensed helium. *Rev. Mod. Phys.*, 67:279, 1995.

[31] A. Ricci and G. Ciccotti. Algorithms for brownian dynamics. *Molec. Phys.*, 101:1927–1931, 2003.

[32] M. F. Herman, E. J. Bruskin, and B. J. Berne. On path integral monte carlo simulations. *J. Chem. Phys.*, 76:5150, 1982.

[33] K. Maki and H. Takayama. Quantum-statistical mechanics of extended objects. I. Kinks in the one-dimensional sine-gordon system. *Phys. Rev. B*, 20:3223, 1979.

[34] S. Coleman. Quantum sine-Gordon equation as the massive Thirring model. *Phys. Rev. D*, 11:2088, 1975.

[35] A.O. Gogolin, A. A. Nersesyan, and A. M. Tsvelik. *Bosonization and strongly correlated systems*. Cambridge University Press, 1998.

[36] P. Chauve, T. Giamarchi, and P. Le Doussal. Creep via dynamical functional renormalization group. *Europhys. Lett.*, 44:110–115, 1998.

[37] M. H. Müser and M. O. Robbins. Conditions for static friction between flat crystalline surfaces. *Phys. Rev. B*, 61:2335, 2000.

[38] J. A. Combs and S. Yip. Single-kink dynamics in a one-dimensional atomic chain: A nonlinear atomistic theory and numerical simulation. *Phys. Rev. B*, 28:6873, 1983.

[39] M. Peyrard and M. D. Kruskal. Kink dynamics in the highly discrete sine-Gordon system. *Physica D*, 14:88, 1983.

[40] T. Strunz and F.-J. Elmer. Driven Frenkel-Kontorova model. II. Chaotic sliding and nonequilibrium melting and freezing. *Phys. Rev. E*, 58:1612–1620, 1998.

[41] G. Krilov and B. J. Berne. Real time quantum correlation functions. II. maximum entropy numerical analytic continuation of path integral monte carlo and centroid molecular dynamics data. *J. Chem. Phys.*, 111:9147–9156, 1999.